This is a non-peer reviewed manuscript, submitted to Science Advances on 26th August 2021.

Title:
Viscous fault creep controls the stress-dependence of modelled earthquake statistics

Authors:
Adam Beall[1]*, twitter: @adambeallgeo
Martijn P.A. van den Ende[2,3], twitter: @martijnende
Jean-Paul Ampuero[2], twitter: @DocTerremoto
Åke Fagereng[1], twitter: @akefagereng

[1]School of Earth and Environmental Sciences, Cardiff University, Cardiff, UK

[2]Université Côte d'Azur, IRD, CNRS, Observatoire de la Côte d'Azur, Géoazur, Valbonne, France

[3]Université Côte d'Azur, OCA, UMR Lagrange, France

Contact email:
adambeall1@gmail.com

Viscous fault creep controls the stress-dependence of modelled earthquake statistics

Short title: Fault creep and stress-dependence of earthquakes

Authors

Adam Beall[1]*, Martijn P.A. van den Ende[2,3], Jean-Paul Ampuero[2], Åke Fagereng[1]

Affiliations

[1]School of Earth and Environmental Sciences, Cardiff University, Cardiff, UK

[2]Université Côte d'Azur, IRD, CNRS, Observatoire de la Côte d'Azur, Géoazur, Valbonne, France

[3]Université Côte d'Azur, OCA, UMR Lagrange, France

[*]Corresponding author. Email: adambeall1@gmail.com

Abstract (150 words)

The ability to estimate the likelihood of particular earthquake magnitudes occurring in a given region is critical for seismic hazard assessment. Earthquake size and recurrence statistics have been empirically linked to stress state, however there is ongoing debate as to which fault-zone processes are responsible for this link. We numerically model combined viscous creep and frictional sliding of a fault-zone, where applied shear stress controls the interplay between these mechanisms. This model reproduces the stress-dependent earthquake magnitude distribution observed in nature. At low stress, many fault segments creep and impede ruptures, limiting earthquake sizes. At high stress, more segments are close to frictional failure and large earthquakes are more frequent. Contrasts in earthquake statistics between regions, with depth and through time, may be explained by stress variation, which could be used in the future to further constrain probabilistic models of regional seismicity.

Teaser (125 characters)

Regional stress influences earthquake statistics by changing the interplay between fault friction and viscous creep.

Introduction

The cornerstone of modern seismic hazard assessment is the ability to model the statistical distribution of how often earthquakes of varying sizes occur in a given region (*1*). This is typically modelled following the Gutenberg-Richter (G-R) relationship, where the number N of earthquakes of moment magnitude M_w or greater that occur in a specific region in a given time period is given by $\log(N) = a - bM_w$, where a and b are empirical parameters. The b-value in this equation varies between regions; for example, for thrust fault earthquakes it is 0.75 at the

Honshu subduction margin (Japan) and 1.07 at the Marianas margin (*2*). A higher b-value indicates that the ratio of large to small earthquake rates is smaller (large earthquakes are relatively less frequent) and is typical of relatively aseismic regions. However, it is difficult to accurately constrain b-values empirically, owing to the long recurrence time of large earthquakes compared to the limited extent of instrumental earthquake catalogues (*1*, *3*, *4*). Constraints on the physical mechanisms controlling b-value variation are needed to reduce such uncertainty.

What controls the b-value is under ongoing debate, and many factors have been proposed including stress, earthquake location and focal mechanism, temporal evolution during the earthquake cycle, inter-seismic deformation and others (summarized by El-Isa and Eaton (*5*)). A high b-value has been linked to low differential stress in laboratory experiments (*6*). In nature, it has been linked to extensional tectonic regimes (*7*), shallow earthquake hypocenters (*8*), regions hosting inter-seismic creep (*9*) and periods following large earthquakes (*10*). These regions and periods are generally associated with relatively low differential stress. Physical models have been developed to understand this empirical link between stress and b-value. The distribution of earthquake sizes described by the G-R relationship is thought to reflect a power-law (fractal) distribution of material properties, fault lengths or stress in the Earth (*6*, *11–16*). An increase in the stress loading a material with a power-law strength distribution results in larger fault areas with stress conditions favorable for frictional failure (*6*, *14*), while still reproducing the G-R relationship, leading to a predicted decrease in b-value. However, this process is complicated by consideration of rupture dynamics and earthquake cycles. Fault shear-stress evolves chaotically as fault segments slip, while also depending on fault loading conditions. Earthquakes may also propagate through regions with stress conditions or material properties that are unfavorable for earthquake nucleation, depending probabilistically on the magnitude and heterogeneity of fault stress and strength (*15*, *17*, *18*). Earthquake cycle models can address these ambiguities by reproducing fault stress states that evolve self-consistently and can be used to study the controls on fault rupture for various fault structures, properties and conditions. Such models have been used to reproduce the G-R relationship (*16*, *19–21*), though an outstanding question is how they can reproduce the b-value dependence on stress.

At regional scales, the differential stresses loading faults are related to the forces that drive mantle convection and plate tectonics (*22*). Tectonic stress can vary significantly, manifesting as contrasts in crustal deformation in the regions adjacent to faults, such as variations in overriding plate shortening behind subduction megathrusts (*23*). These contrasts imply that faults deform at varying stresses (*24*, *25*). The behavior of fault-zone deformation that results from this loading stress depends on fault rheology. Within the seismogenic zone, fault-zone deformation is accommodated by combinations of stable viscous creep and either stable or unstable frictional slip (*26*), where rapid unstable slip corresponds to earthquake nucleation and propagation. The viscous and frictional mechanisms each interact with the fault stress state, which is in turn linked to tectonic loading. For example, a fault region with viscously weak materials may creep sufficiently to accommodate regional fault slip, sustaining a relaxed shear stress that is too low for frictional deformation to dominate. Should regional stress increase, creep may be unable to accommodate the faster or more localized regional fault slip, driving local elastic strain accumulation, stress increase and a switch to frictional deformation. Such visco-frictional interactions influence the evolving fault stress field and subsequently the behavior and statistics of earthquake ruptures (*20*).

Geological and geophysical inferences indicate that strength and stress vary within plate interface fault-zones, possibly providing the mechanical heterogeneity required to reproduce the G-R relationship in models. Exhumed natural fault-zones appear to have deformed by spatially

heterogeneous combinations of localized frictional sliding and distributed viscous creep ((*27–29*), Fig. 1a). At the 100 km scale, some fault segments appear to accommodate permanent deformation (at present day) without accumulation of elastic strain in geodetic inversions (*26*, *30*, *31*), and are interpreted as weak, creeping zones. Subduction zone megathrusts with a large proportion of creeping material commonly occur where the hanging wall is experiencing extension (*32*), implying low tectonic differential stress. Weak phyllosilicates have been found in a creeping section of the San Andreas fault (*33*). Creeping regions may also act as 'barriers' to earthquakes, promoting their arrest, which is also consistent with relaxed stress (*30*). 'Locked' regions that do not host inter-seismic creep instead may act as 'asperities', which fully rupture in potentially large earthquakes (*34*). As loading stress controls whether creep or frictional failure occur, the distribution of creeping and locked regions may be modified by changing tectonic stress conditions (*9*, *35*).

We hypothesize that changes to the relative proportions of creeping and frictional materials in a fault-zone, linked to variations in shear stress, may result in changes to the b-value and explain its stress-dependence. We test this by using the numerical modelling code QDYN (*36*) to develop models of fault deformation occurring by a combination of frictional sliding and viscous creep. Complex visco-frictional fault-zones in nature are represented as a coupled fault and shear-zone (Fig. 1a-b), allowing us to explore how stress relaxation due to shear-zone deformation influences the size of earthquakes hosted on the fault. We model earthquake cycles that involve a range of rupture dynamics that depend on this visco-frictional interplay. The resulting catalogue of models reproduce the relationship between stress and b-value, as well as typical ranges of maximum M_w and inter-seismic coupling. Our models provide a way of linking earthquake statistics to possible underlying variations in fault properties and stress state, and imply that aseismic fault-zones may be dominated by the combined presence of creeping materials and low tectonic stress. By constraining the interplay between seismicity, rheology and tectonic stress, we work towards the integration of tectonic characteristics into earthquake cycle models and therefore an improved understanding of regional probabilistic earthquake models.

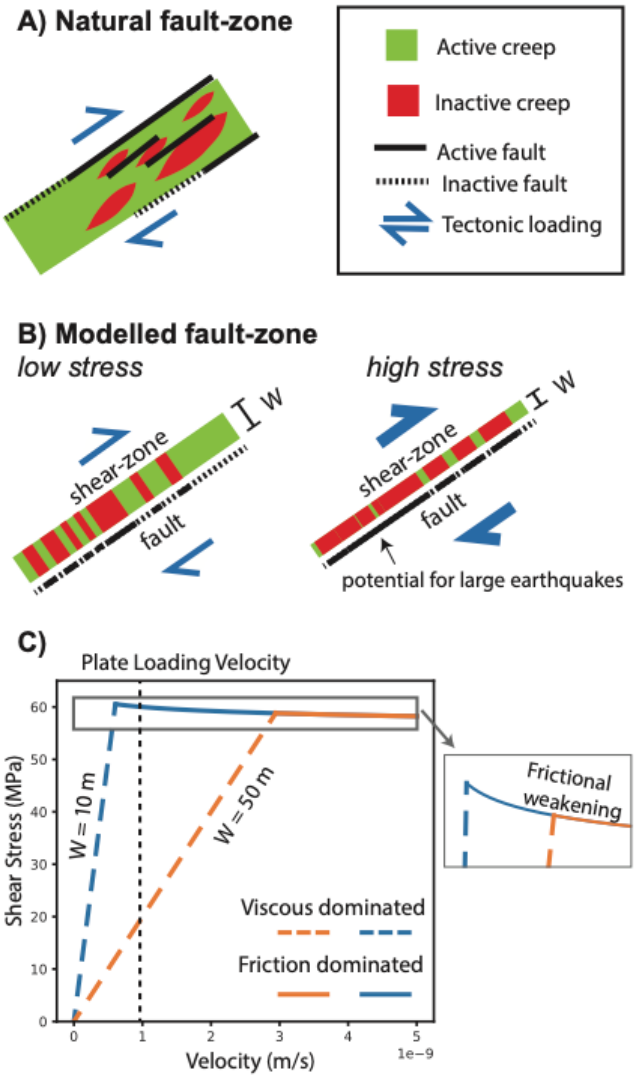

Fig. 1. Schematic of natural and modelled fault-zones (A-B), with rheology (C). Natural fault-zones (A) typically consist of a mixture of frictional and creeping parts, which are modelled here (B) as a combined shear-zone and fault system that becomes increasingly friction-dominated at high stress. The interplay between viscous creep and rate-and-state friction is shown schematically in shear strength vs slip velocity curves (C). Viscous creep cannot accommodate plate velocities in the thin shear-zone example (W = 10 m). The fault with a thicker shear-zone must slip at least at 3x the plate velocity for frictional slip to dominate, below which it deforms at low stress.

Results

Stress-dependent Rupture Dynamics

We present a reference model-set which reproduces similar earthquake characteristics to natural observations. All modelled faults are uniformly velocity-weakening, such that they would be highly seismogenic in the absence of viscous creep. The fault consists of 10-100 m wide patches, each with Newtonian viscosity η that is randomly chosen (following a logarithmically uniform distribution). A maximum viscosity contrast of 100 is prescribed, reflecting heterogeneity within

the seismogenic zone inferred in nature (*28*, *37*) and from microphysical models (*38*). Each fault element is composed of frictional and viscous mechanisms in series, such that the weakest one dominates deformation. At low stress, viscous deformation is dominant (Fig. 1b). A higher stress is required for relatively slow frictional sliding to dominate, as is required for earthquake nucleation to occur. At steady-state seismic slip velocities, frictional sliding occurs at reduced stress due to dynamic weakening, however the fault must strengthen again for subsequent earthquakes to nucleate.

Shear-zone thickness W is the only parameter that is varied, which acts to control strain-rate $\dot{\gamma}$ (for a given slip rate v, $\dot{\gamma} = v/W$) and thus viscous strength ($\tau = \eta\dot{\gamma}$). A large W lowers the strain-rate, making creep more efficient and lowering the stress that the fault-zone can deform at (Fig. 1b,c). While we change W to control fault background stress, this may also represent the converse relationship of background stress in geodynamic models leading to variations in shear zone thickness (*39*). By varying W between 10 and 1000 m, we can reproduce an average fault stress that reaches a maximum τ_{max} during the earthquake cycle that ranges from 19 to 49 MPa in different models (Fig. 2). Despite this variation, earthquake stress drops are relatively constant ~10 MPa (Fig. S1), consistent with seismological observations (*40*).

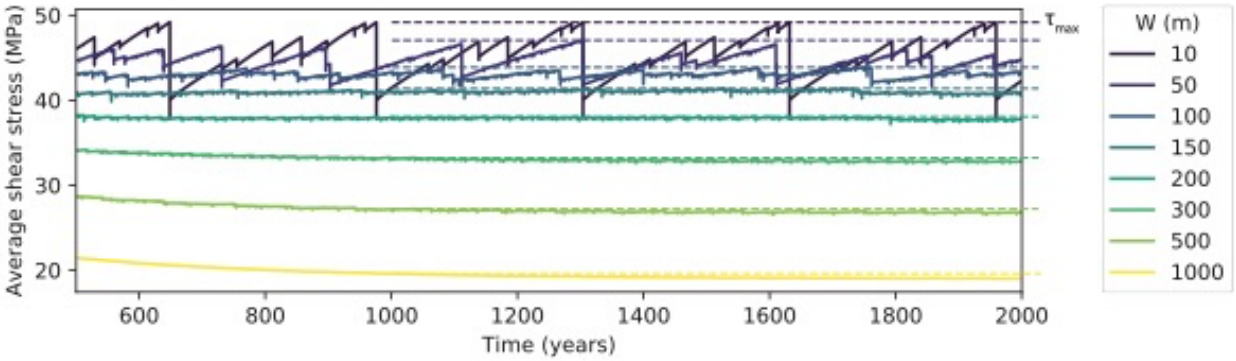

Fig. 2. Shear stress through time for the reference model-set. Stress is averaged over the entire fault and the maximum shear stress τ_{max} is shown with dashed lines.

At relatively low stress (reproduced using large W), such as for Fig. 3a, earthquakes are generally limited to isolated regions of high viscosity and are consequently restricted to low magnitudes ($M_w < 5.7$ and on average $M_w \sim 4$). Defining an asperity as a friction-dominated area, where earthquakes nucleate, 'effective asperities' are predicted as areas where the stress required for creep to accommodate the loading slip rate is greater than the steady-state frictional strength, over lengths larger than the earthquake nucleation length-scale (the black stripes at the bottom of each panel in Fig. 3). At low stress, earthquakes are predominately limited to each of these effective asperities, rarely propagating into adjacent creeping regions or spanning multiple asperities.

With decreasing W (and correspondingly increasing stress), the effective asperity sizes increase (Fig. 3b-c). The larger effective asperities correspond to fault regions hosting larger earthquakes, that also occasionally span multiple asperities. Small earthquakes also persist, both hosted on small asperities and occurring as partial ruptures of larger asperities, nucleating on patches with particularly high viscosity. When $\tau_{max} = 47$ MPa (W = 50 m), earthquakes with $M_w < 6.9$ occur, due to ruptures that propagate over large effective asperities as well as small intervening regions (~ 1 km wide) of low viscosity that are otherwise dominated by inter-seismic creep (e.g. at 15-20 km in Fig. 3c). Large events occur less frequently than small events and with greater

displacement, as occurs in natural scaling relationships. The largest events in the reference model-set are $M_w < 7.4$ and are limited by the fault length. We ran the reference model-set three times with different randomized viscosity distributions. Both maximum stress τ_{max} and maximum magnitude M_w can vary for a given W, though we will show that the characterization of seismogenic behavior in terms of τ_{max} is robust.

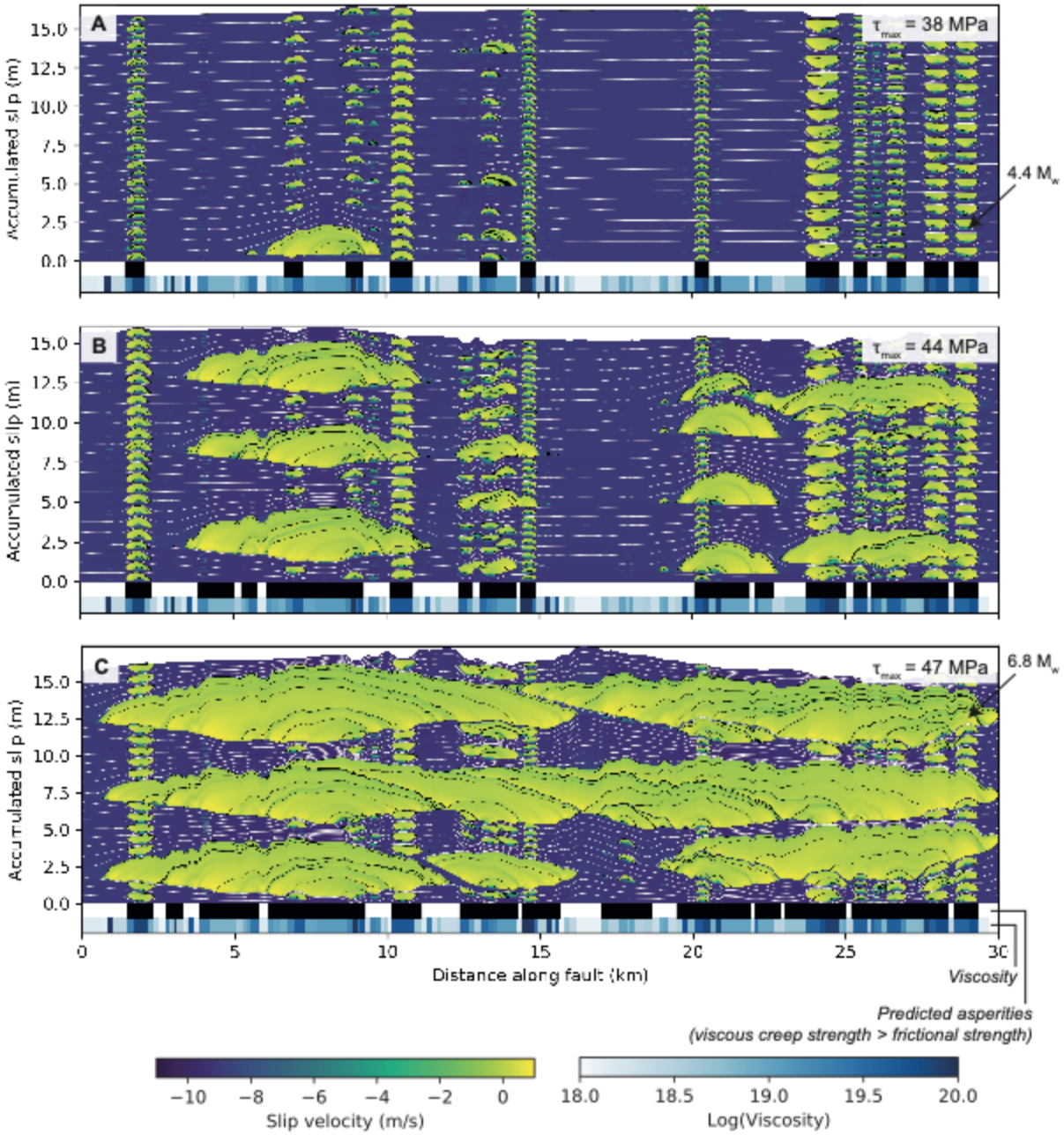

Fig. 3. Modelled seismic and inter-seismic slip. Accumulated slip over 500 years for reference models with W = 200, 100 and 50 m (A-C), with seismic slip in yellow and creep in purple. White curves are separated by inter-seismic intervals of 20 years and black curves by seismic intervals of 2 seconds. Below each plot, the distributions of viscosity (identical between models) and effective asperities are shown.

Earthquake Statistics

The model statistics are described in terms of τ_{max} (a model output), the range of which is produced by varying W, as the seismogenic behavior is later shown to be generalized in terms of fault stress for all models (which also holds for time-averaged stress, but not W, Fig. S2) and long-term fault stress is the quantity linked to tectonics. We firstly describe the maximum M_w and seismic coupling χ, which is calculated as the ratio of the total accumulated seismic slip to the total loading displacement, over the analyzed model period. Both maximum M_w and χ show a clear trend of increase with stress (Fig. 4a-b). This increase is gradual over the range τ_{max} = 20 – 40 MPa and more rapid at greater stress. We define an aseismic model as being characterized by $\chi < 0.3$ and maximum $M_w < 6$. While there is no agreed definition of aseismic behavior, as seismicity is pervasive in the Earth's crust, these values are typical of less seismogenic subduction zones (*2*, *31*). Models with τ_{max} < 40 MPa are then relatively aseismic, while becoming increasingly seismogenic at higher stress.

We calculate b-values for the reference model-set by combining the randomized model realizations into single, more statistically complete, catalogues for each modelled W. The recurrence times of seismic events are reasonably approximated by the G-R relationship (Fig. 5). The b-value increases with increasing W and correspondingly decreasing τ_{max}, reflecting the decreased likelihood of large events with decreasing stress. The b-value becomes relatively constant at ~1.5 for $\tau_{max} \leq 34$ MPa ($W \geq 300$ m), within uncertainty (Fig. 4c), which we characterize as aseismic, in agreement with the characterization based on maximum M_w and χ. At the highest stress ($\tau_{max} = 48$ MPa) there are fewer events with $M_w \gtrsim 7$ than expected from the G-R relationship, as larger events are prevented by the imposed fault length (exploratory models with longer faults host larger events, Fig. S3). There are also fewer events with $5 < M_w < 6$ than expected at low stress ($\tau_{max} \leq 38$ MPa), likely due to a reduction in the seismic energy budget due to fault creep. Most b-values are within the range of b-values compiled by Nishikawa and Ide (*41*) for subduction zones and all are within the wide range reported in the literature for all settings (*5*).

The models can be characterized more generally in terms of the non-dimensional pre-stress ratio $\bar{\tau}_0$, which measures the available static stress drop, relative to the strength drop (which is also the maximum possible stress drop). It is calculated as $\bar{\tau}_0 = (\tau_0 - \tau_d)/(\tau_s - \tau_d)$, for pre-seismic stress τ_0 (here taken as τ_{max}) and static and dynamic frictional strengths τ_s and τ_d (defined as the strength during steady-state sliding of 1e-9 m/s and 1 m/s respectively). The greatest change in seismogenic behavior occurs in the stress range 40 to 50 MPa, corresponding to a range of $\bar{\tau}_0$ = 0.13 to 0.57 (Fig. 4c). Variation of $\bar{\tau}_0$ within the fault is shown by the statistical distributions in Fig. 4d, which demonstrate that when $\bar{\tau}_0 < 0.13$ a large proportion of the fault has a negative available stress drop ($\bar{\tau}_0 < 0$), promoting rupture arrest. There are always localized parts of the fault reaching τ_s ($\bar{\tau}_0 = 1$), driving earthquake nucleation.

We tested the sensitivity of our results to the imposed viscosity probability distribution, using additional model-sets (symbols in Fig. 4a-c) with smaller or larger viscosity contrasts, or following power-law or bi-modal (either high or low viscosity) distributions. Each model-set reproduces a dependence of earthquake statistics on stress, while the sharpness of the transition in seismogenic behavior increases for lower viscosity contrasts or bi-modal viscosity.

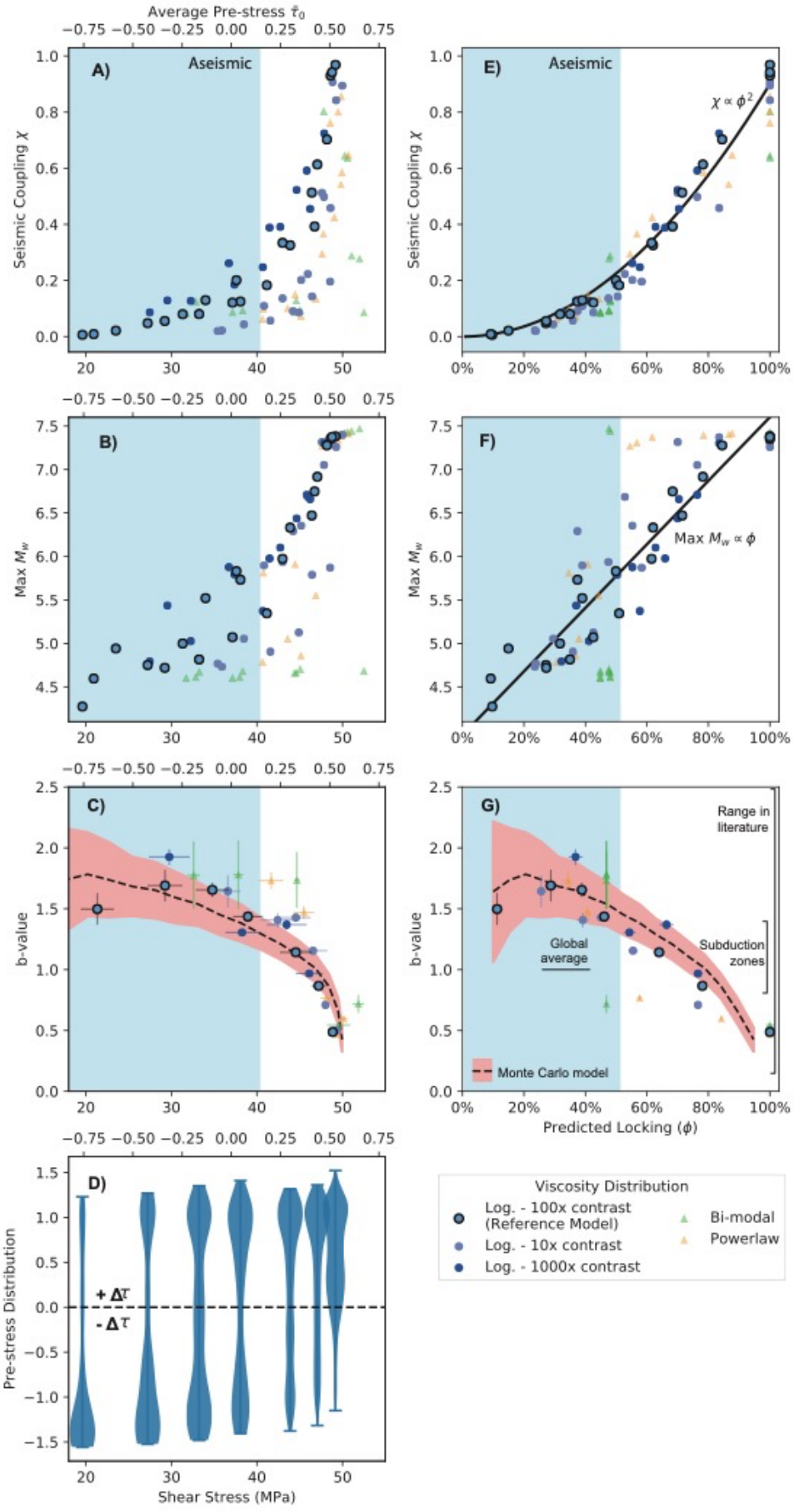
Average Pre-stress $\bar{\tau}_0$
A)
Aseismic
Seismic Coupling χ
B)
Max M_w
C)
b-value
D)
Pre-stress Distribution
+ $\Delta\bar{\tau}$
- $\Delta\bar{\tau}$
Shear Stress (MPa)
E)
$\chi \propto \phi^2$
F)
Max $M_w \propto \phi$
G)
Range in literature
Global average
Subduction zones
Monte Carlo model
Predicted Locking (ϕ)
Viscosity Distribution
Log. - 100x contrast (Reference Model)
Log. - 10x contrast
Log. - 1000x contrast
Bi-modal
Powerlaw

Fig. 4. Earthquake statistics for all model-sets. The reference model-set is indicated by outlined circles. The mean ± standard deviation of b-values in a Monte Carlo simulation with isolated effective asperities is shown in pink in panels C and G. The distribution of the non-dimensional pre-stress ratio $\bar{\tau}_0$ at the time of maximum fault shear stress is shown for the reference model-set (D), where fault segments may have positive or negative available stress drop $\Delta\tau$.

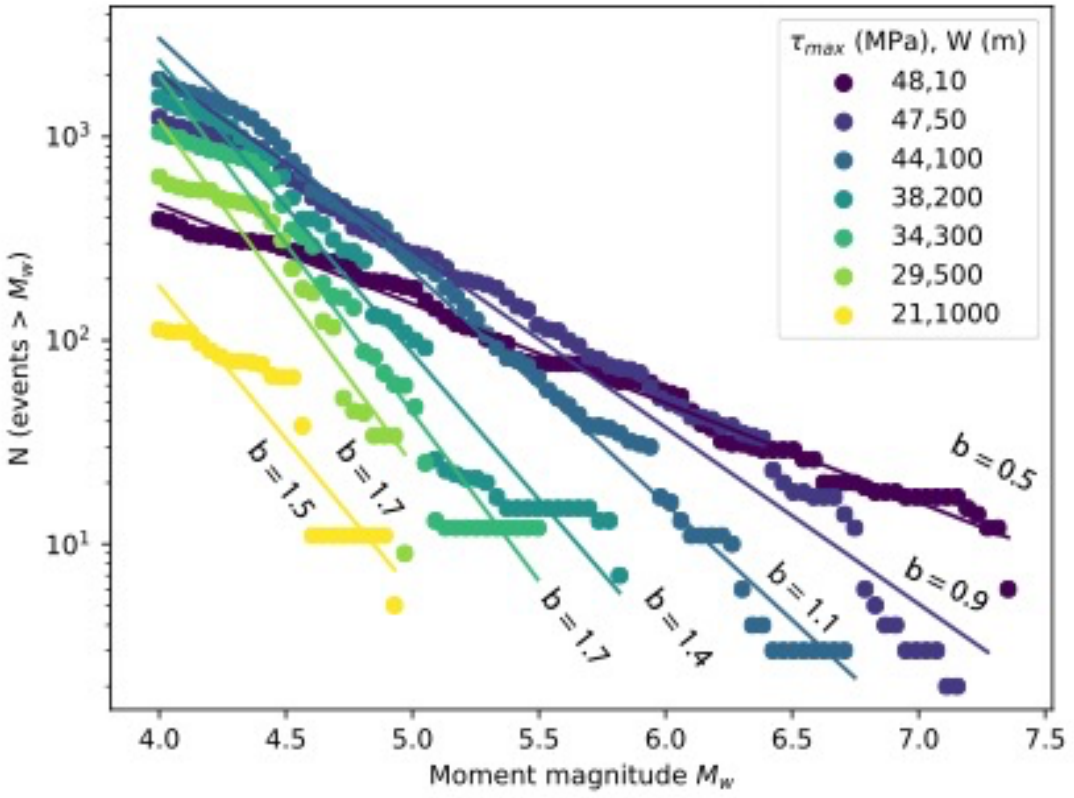

Fig. 5. Earthquake size statistics for models operating at different maximum stress. The modelled seismic events, collected over a 1500 year period, approximately follow the Gutenberg-Richter power-law relationship, where the fitted b-value varies across the reference model-set.

We also quantify how visco-frictional interplay influences seismogenic behavior by plotting the statistical data as a function of the proportion of the fault-zone that is locked (Fig. 4e-g), ϕ, estimated as the proportion of the fault comprising effective asperities. In comparison to seismic coupling χ, which measures how much displacement is frictional in the model runs, ϕ is an estimate of how much area of the fault is expected to be frictional based on steady-state rheological behavior (ignoring episodic frictional behavior of creeping segments). From this perspective, the change in seismogenic behavior occurs more gradually and systematically, with maximum $M_w \propto \phi$ (for $\phi \leq 0.8$), $b \propto -\phi$ (approximately, for $\chi \geq 0.4$) and $\chi \propto \phi^2$. For constant stress drop, χ is proportional to the sum of the squared rupture lengths l_r^2 for all events. The parabolic relationship between χ and ϕ can then be explained if every effective asperity increases linearly in size with increasing overall locking area, which appears to approximately be the case in Fig. 3. The linear relationship between maximum M_w and ϕ implies that the seismic moment M_0 scales exponentially with ϕ, which may potentially reflect an accelerated coalescence of

frictional fault segments with increasing ϕ, though there is no obvious clear explanation for this scaling.

Linking b-values and effective asperity sizes

The b-value variation with stress can be related to the growth of effective asperities with increasing stress. While the imposed patch sizes follow a power-law, different combinations of these patches combine into the effective asperities for varying τ_{max}. The size distribution of the effective asperities still follows a power-law for each W, with the power-law exponent decreasing with increasing stress (Fig. S4). The effective asperity size distributions can be converted to predicted event catalogues by assuming that each earthquake is confined to an isolated effective asperity, as is generally the case at low τ_{max} (Fig. 3), that all events have a constant stress drop and that the stressing rate of an asperity is inversely proportional to its size (such that small asperities host events more regularly). The b-values for these predicted events agree with the modelled events, indicating that the effective asperity size distributions play a role in the stress-dependence of the b-value (Fig. S4).

We use this method of predicting the b-value from the effective asperity distribution to test the sensitivity of our b-value calculations to the randomized fault viscosity, using a Monte Carlo simulation involving 10^4 synthetic effective asperity distributions. The mean b-values of this catalogue (dashed line, Fig. 4c) agree well with the b-values calculated for the full earthquake cycle models, while the observation of decreasing b-value with increasing stress is robust within the uncertainty highlighted by the standard-deviation (pink region). Having focused on small ruptures that are confined to effective asperities, we next explore how large ruptures span multiple asperities.

The role of viscosity contrast in controlling rupture arrest

Ruptures become increasingly capable of propagating through creeping regions as τ_{max} increases (Fig. 3). We use a simplified numerical model to understand this behavior, consisting of a single asperity surrounded by a uniformly low-viscosity 'matrix' material. Ruptures nucleating on the patch propagate into the matrix to varying distances, depending on the patch width and matrix viscosity. For a matrix that can creep at stress lower than dynamic frictional strength ($\bar{\tau}_0 < 0$, negative available stress drop), rupture arrest occurs after less than 1 km of rupture propagation into the matrix, even when the asperity is as wide as 15 km. For a pre-stress $0 < \bar{\tau}_0 < 0.55$, rupture propagation can reach 1 km or greater into the viscous matrix (Fig. 6). This range coincides with the range of most significant change in seismogenic behavior in Fig. 4 ($\bar{\tau}_0$= 0.13 to 0.57). Ruptures occurring in this stress range can only penetrate the matrix by a small proportion of the asperity width, in agreement with the ruptures in Fig. 3b. At $\bar{\tau}_0 \geq 0.55$, whole fault rupture (no arrest until the model edges) can occur, provided the patch width is greater than a critical value that decreases with increasing $\bar{\tau}_0$. This $\bar{\tau}_0$ threshold agrees with the stress at which the largest ruptures ($M_w > 7$) are limited by the imposed fault length in Fig. 4b. This threshold also agrees with the ~90% likelihood of whole-fault rupture on the roughest fault modelled by Fang and Dunham for $\bar{\tau}_0$~0.5 (*17*).

To further examine this rupture behavior we use an analytic energy balance calculation, which predicts that rupture arrest occurs when there is insufficient available stress drop (i.e. $\bar{\tau}_0$) at the rupture front to drive further rupture propagation (*15*). This calculation broadly reproduces the dependence of rupture penetration on both matrix viscosity and patch width, for relatively narrow patch widths, and dependence primarily on viscosity for the widest patches. However, ruptures

arrest more rapidly in the numerical models than estimated by the energy balance calculation. This is because $\bar{\tau}_0$ tends to be lower than expected for steady-state creep, as stress shadows form adjacent to locked patches.

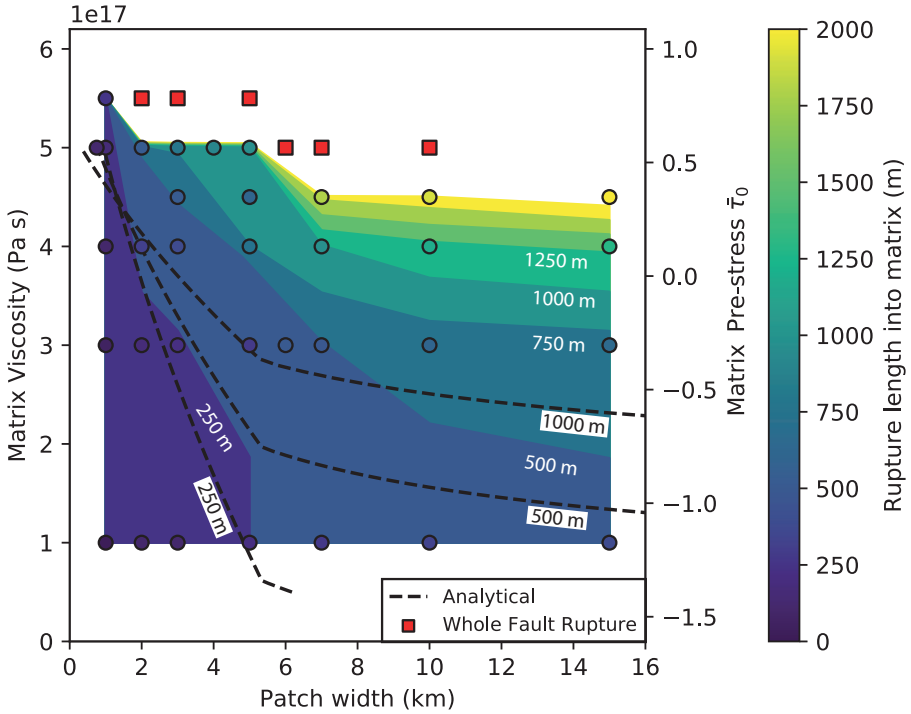

Fig. 6. Distance of rupture penetration into the viscous matrix in simplified single patch models. Each point results from a separate model, colored by the distance the largest rupture propagates from one asperity edge into the matrix. The data are shaded between interpolated contours in intervals of 250 m. The solution to an energy balance calculation (dashed lines), predicts the conditions for arrest at a variety of distances, though generally underestimates rupture length.

Stress-dependence of the frictional-viscous transition

The visco-frictional fault-zone model developed here has the capability of linking variations in tectonic stress to earthquake statistics. We demonstrate this by reproducing the decline in seismicity with depth typically observed near the frictional-viscous transition, using an idealized subduction zone thrust model, and relate this to stress relaxation by creep at high temperature. We then use this model to study how the brittle-ductile transition may respond to a change in large-scale background stress. Depth-dependent stress is introduced to the reference model-set, simply by scaling the viscosity distribution by a depth-dependent factor that mimics the Arrhenius temperature-dependence of typical rheology. This simplified viscosity distribution may represent a transition from pressure-solution creep of only some lithologies within much of the seismogenic zone (*37*), to bulk weakening of most lithologies at higher temperatures(*27*). We ignore the variation of frictional properties and normal stress with depth, in order to isolate the influence of viscous creep on the frictional-viscous transition.

A generic megathrust geometry is chosen, with a slab dip of 20° (global average (*42*)), depth range of 10 – 45 km and a rheological visco-frictional transition at the mid-depth (27.5 km). Two

models are analyzed, representing lower and higher tectonic stress, by assuming a high and low W respectively. In the absence of depth-dependent viscosity, the lower and higher stress models have τ_{max}= 43 MPa and 47 MPa respectively, near the lower and higher ends of the pre-stress range required to reproduce a variety of seismogenic behavior ($\bar{\tau}_0 = 0.26$ and 0.43; Fig. S3).

The upper half (above 27.5 km) of the lower stress model (Fig. 7a) hosts earthquakes ranging from M_w ~ 3 to 7, with a b-value of 1.1 and χ = 0.4 (Fig. S5). The viscosity is lowered with increasing depth (keeping the local maximum viscosity contrast constant) from a depth of 27.5 km. This viscosity reduction results in a transition to aseismic deformation, with no events with $M_w \geq 5$ at depths > 30 km. At these depths much of the fault has a viscosity low enough to accommodate steady creep (red line, Fig. 7c). This lower half of the fault has a higher b-value of 1.7 and χ = 0.1. Isolated events with M_w ~ 4 events occur at 40 km depth, hosted on a patch of high viscosity. The largest events, $M_w = 7$, propagate only partly (~7 km depth) into the low viscosity zone, before arresting. Fault shear stress variation with depth is shown and smoothed to represent the stress state away from the fault, which would be in equilibrium with the tectonic stress state. This fault stress declines in the lower half of the fault, reflecting the decreased viscosity and reproducing the broad transition to aseismic deformation in nature.

The higher stress subduction thrust model is shown in Fig. 7b. The fault shear stress is more spatially uniform in the shallow section and only mildly decreases with decreasing viscosity in the lower temperature-dependent section. Only isolated patches have low enough viscosity to accommodate steady creep (Fig. 7c). The appearance of greater shear stress variation through time is due to earthquakes occurring over greater areas, while stress changes due to smaller events in the low stress model were smoothed out. This high stress fault-zone hosts two $M_w > 8$ events, which propagate well into the region of decreased viscosity, almost 15 km deeper than in the low stress model. These large events are 'characteristic earthquakes' that are distinct in size and occur more frequently than expected from the G-R relationship (Figs. S2 and S8). Earthquakes occur throughout the model domain, with M_w~5 events occurring as deep as 40 km. The change in earthquake statistics with depth is also more gradual than the low-stress model, with a transition from b = 1.0 to 1.3 and χ = 0.8 to 0.5 between the upper and lower (above and below 27.5 km) halves of the fault. These characteristics all indicate that the change in background stress is sufficient to host larger events in the seismogenic zone and shift both the lower extent of the seismogenic zone and the brittle-ductile transition downward substantially.

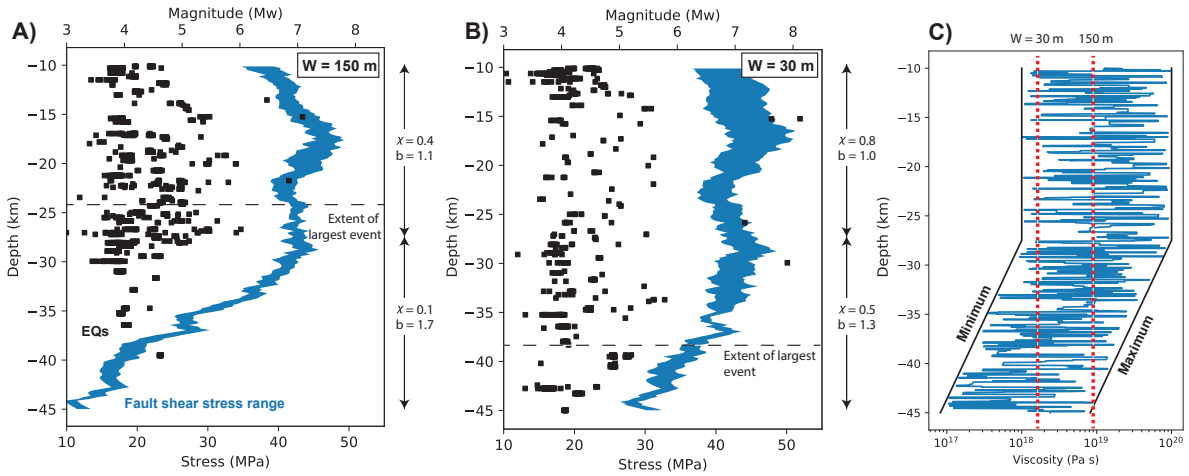

Fig. 7. Modeling the brittle-ductile transition using a depth-dependent viscosity. A decrease in shear stress in the lower half of the 'low stress' model (A, W=150 m) results in a transition to aseismic fault deformation at depth, while most of the fault in the 'high stress' model (B, W=30 m) is seismogenic. The minimum and maximum shear stresses that occurred over the 1500 years model time are shown (shaded blue). An identical depth-dependent viscosity distribution is used for both models (C), where the minimum viscosity required to accommodate the plate slip velocity v_p by creep are shown in red.

Discussion

The modeling presented here has analyzed the underlying mechanism responsible for variation of b-value with stress, as observed experimentally and in nature. Models have previously demonstrated a link between stress heterogeneity and earthquake statistics, where heterogeneous fault stress relates to variation in earthquake size (*6*, *14–17*, *19*, *20*, *43*). A fault with significant stress variation must be loaded to a high stress in order for an earthquake rupture to grow to a large magnitude, which is interpreted as implying that static fault properties, such as roughness, control both rupture characteristics and fault stress (*17*). Loading stress varies depending on tectonic setting and therefore must also be a variable that can contrast between faults. Huang and Turcotte (*14*) used a model of power-law-distributed frictional strength to demonstrate how loading stress can influence the b-value, though this model ignored temporal variation of fault stress and strength. Dublanchet (*19*) explored the influence of stress, varied by changing effective normal stress, on b-value in a rate-and-state earthquake cycle model, however found that this simultaneously affects the nucleation length and leads instead to an increase in b-value with increasing stress. We have modelled earthquake cycles on a fault-zone that can be loaded at varying regional shear stresses, as creep mechanisms accommodate deformation in fault regions where the stress never reaches sufficient magnitudes to cause significant frictional sliding. By using this method to load a fault to varying shear stresses, we can successfully reproduce the relationship between b-value and shear stress, without invoking any variation in frictional properties.

The distribution of asperities and creeping regions on subduction megathrusts has been associated with geometrical and rheological heterogeneity at length scales of 100 m to 1 km (*44*), which correspond to our modelled patches. Large earthquakes can span distances of 10-100 km and variation in seismogenic behavior has been linked to geometric heterogeneity at such large wavelengths (*45*). Alternatively, large earthquakes may be hosted on many small asperities which

rupture collectively at high stress (*9*), corresponding to our modelled effective asperities. In this case, the distribution of earthquake sizes and nucleation sites depends on a combination of inherited properties at small scales and tectonic stress at larger scales. There is subsequently uncertainty in using the extent of asperities to constrain the maximum M_w, as they may change effective size or link together with changing stress, particularly following changes to the regional fault stress state throughout the earthquake cycle.

These models indicate deterministic relationships between b-value, χ, maximum M_w and stress, where the greatest variation in seismogenic behavior occurs over a range of 40 to 50 MPa shear stress, or $\bar{\tau}_0$ = 0.1 to 0.5. This stress range is smaller than previous ~100 MPa order estimates based on regional tectonic stress (*8*, *46*), reflecting instead the lower shear stress that plate interfaces locally operate at (*47*). Geodynamic estimates indicate a ~20% variation in plate interface shear stress (*24*, *39*), such that a variety of geodynamic regimes could span the modelled seismic-aseismic transition. Changes of ~10 MPa are also comparable to stress changes during the earthquake cycle and temporal variation of the b-value has been hypothesized (*48*). Such variations are difficult to measure in nature with statistical significance, but have been demonstrated in experiments (*49*). As the non-dimensional stress $\bar{\tau}_0$ is independent of the frictional strength and strength drop, the seismogenic behavior predicted in the models can be generalized if $\bar{\tau}_0$ can be determined. The degree of creep heterogeneity is also important, as the range over which seismogenic behavior changes narrows by 50% for the smaller viscosity contrasts modelled, corresponding to 'smooth' fault-zones with more homogeneous rheology. Determination of long-term $\bar{\tau}_0$ and rheological heterogeneity can then lead to calibration of the relationship between tectonic stress and earthquake statistics, helping reduce the uncertainty in b-value and M_{max}.

The base of the seismogenic zone is commonly considered as relating to a temperature-dependent transition in rate-and-state parameters (*50–52*). Such transitions involve negligible shear stress variation, given the logarithmic rate dependence of the rate-and-state equations. Alternatively, the seismogenic zone may coincide with the geological frictional-viscous transition, which involves a switch to distributed creep at depth (rather than stable frictional sliding) and a decline in shear stress (*53*, *54*). Our model allows such a transition to be reproduced, where an increasing efficiency of temperature-dependent creep at depth results in decreasing shear stress, decreasing M_w, eventually declining to predominately aseismic creep, and a limit in the down-dip propagation of large earthquakes. We have also shown that increasing the driving stress of the entire fault, representing contrasts in regional tectonic stress, is predicted to shift the brittle-ductile transition downward. The lower extent of seismogenic zones in nature varies considerably; it is thought to reach 15 km at the Mariana margin (*55*), 25-30 km in Nankai (*56*) and 50 km in Sumatra (*57*). This range of transition depths could be partly explained by contrasts in driving stress, where the Mariana and Sumatra are low and high stress end-members respectively, as has been previously suggested on account of their contrasting back-arc deformation styles (*23*, *31*).

We have demonstrated that a fault with a heterogeneous distribution of viscously creeping and frictionally locked patches can host earthquakes that follow the G-R relationship, and that the decreasing contribution of creep at higher driving stresses can explain the empirically determined link between b-value and stress. We show that the frictional-viscous transition can correspond to the increasing dominance of fault creep with depth, occurring at a depth that shifts down with increased regional driving stress. We estimate that a significant contrast in seismogenic behavior can be caused by non-dimensional stress variations of $\Delta\bar{\tau}_0 \approx 0.4$ (dimensionalized here as 10 MPa), which is a sufficiently small stress contrast for seismogenic behavior to vary spatially between tectonic settings. These model applications are preliminary, but highlight the potential to

apply earthquake cycle models that incorporate inter-seismic creep in understanding regional contrasts in seismogenic behavior and earthquake statistics. This modelling approach may then allow knowledge of tectonic stress to further constrain b-value uncertainty and maximum M_w, which are critical for hazard assessment.

Materials and Methods

Earthquake cycle modeling

The boundary element quasi-dynamic earthquake cycle modeling code QDYN (*36*) is used to model visco-frictional deformation of a 1D thrust fault, of length l_{fault} = 30 km, embedded between two elastic half-spaces. Unbounded extensions of the fault beyond the discretized fault domain are loaded by a prescribed slip velocity of v_p =10^{-9} m s^{-1}, representing plate motion. Total fault slip is assumed to be the sum of viscous (v_v) and frictional (v_f) slip rates, such that the weakest mechanism dominates. This implies that at any given point on the fault we have (for bulk shear stress τ and frictional and viscous stresses τ_f and τ_v):

$$\tau = \tau_f = \tau_v \quad (1)$$

$$v = v_f + v_v \quad (2)$$

Viscous deformation is assumed to follow Newtonian viscous creep, for shear zone thickness W and viscosity η:

$$v_v = \frac{\tau W}{\eta} \quad (3)$$

Frictional deformation is assumed to follow the regularized form of rate and state friction (*58*), which allows the frictional slip rate to vanish (when creep dominates) and can be written as:

$$v_f = 2v_0 \, sinh\left(\frac{\tau}{a\sigma}\right) exp\left(-\frac{1}{a}\left[\mu_0 + b \, ln\left(\frac{v_0\theta}{Dc}\right)\right]\right) \quad (4)$$

Where σ is the effective normal stress, a is the direct effect parameter, b is the evolution effect parameter, D_c is a characteristic slip distance which governs the evolution of the state parameter θ, and v_0 is a reference velocity at the corresponding shear stress $\mu_0\sigma$. Finally, we take the aging law to describe the state evolution:

$$\frac{d\theta}{dt} = 1 - \frac{v\theta}{D_c} \quad (5)$$

QDYN adopts the quasi-dynamic approximation by Rice (1993), with the associated force balance:

$$\frac{d\tau_i}{dt} = K_{ij}\left(v_{pl} - v_j\right) - \frac{G}{2c_s}\frac{dv_i}{dt} \quad (6)$$

In which K_{ij} is a stiffness matrix that relates the change in shear stress on the i-th fault element (τ_i) to slip on the j-th fault element (v_j) (the Einstein summation convention is adopted here). The last term on the right-hand side represents the stress change due to seismic wave radiation normal

to the fault plane, and comprises the shear modulus of the medium G and the shear wave speed c_s, which are both uniform and constant in the simulations.

In order to connect the force balance with the point-wise fault rheology, we expand the equation for slip rate into its partial derivatives:

$$\frac{dv_i}{dt} = \frac{\partial v_i}{\partial \tau}\frac{d\tau_i}{dt} + \frac{\partial v_i}{\partial \theta}\frac{d\theta_i}{dt} = \left(\frac{\partial v_{f,i}}{\partial \tau} + \frac{\partial v_{v,i}}{\partial \tau}\right)\frac{d\tau_i}{dt} + \frac{\partial v_{f,i}}{\partial \theta}\frac{d\theta_i}{dt} \tag{7}$$

Substitution into the force balance and rewriting then gives:

$$\frac{d\tau_i}{dt}\left(1 + \frac{\partial v_{f,i}}{\partial \tau} + \frac{\partial v_{v,i}}{\partial \tau}\right) = K_{ij}\left(v_{pl} - v_j\right)\frac{\partial v_{f,i}}{\partial \theta}\frac{d\theta_i}{dt} \tag{8}$$

The partial derivatives in this relation are readily obtained from the rheological model, and read:

$$\frac{\partial v_{f,i}}{\partial \tau} = \frac{2v_0}{a\sigma} cosh\left(\frac{\tau_i}{a\sigma}\right)\left(-\frac{1}{a}\left[\mu_0 + b\, ln\left(\frac{v_0\theta_i}{Dc}\right)\right]\right) \tag{9}$$

$$\frac{\partial v_{v,i}}{\partial \tau} = \frac{W}{\eta} \tag{10}$$

$$\frac{\partial v_{f,i}}{\partial \theta} = -\frac{bv_{f,i}}{a\theta_i} \tag{11}$$

Using an adaptive Runge-Kutta solver, at each time step, we solve for the collection of fault variables $X_i = [\tau_i, \theta_i]$ as the solution of:

$$\frac{d\boldsymbol{X}}{dt} = \boldsymbol{F}(\boldsymbol{X}) \tag{12}$$

Finally, we note that for parallel operation of frictional slip and ductile creep, it is necessary to solve for τ and θ and compute $v = f(\tau, \theta)$, rather than solving for v and θ and computing $\tau = g(v, \theta)$, which is a common choice in the modelling community. The reason for this is that it is non-trivial to satisfy the hard constraint $\tau = \tau_f = \tau_v$ while solving for v in the latter approach.

Fault-zone parameters

W is the only parameter that is varied between models in a model-set, and model-sets vary only by the random realization of the distribution of η. The fault consists of patches of width w, which are capped between w_{min} = 100 m and w_{max} = 1000 m and follow a truncated power-law in-between (*20*):

$$P(>w) = 1 - \frac{w^{-D} - w_{min}^{-D}}{w_{max}^{-D} - w_{min}^{-D}} \quad (13)$$

Each patch has a uniform η, sampled from a log-uniform distribution, for $\eta_{min} = 10^{18}$ Pa s, $\eta_{max} = 10^{20}$ Pa s and a uniformly random variable $\hat{X}$ (varying between 0 and 1):

$$\eta = \eta_{min} \left(\frac{\eta_{max}}{\eta_{min}}\right)^{\hat{X}} \quad (14)$$

We assume the frictional parameters $a = 9\text{e-}3$ and $b = 2\text{e-}2$, characteristic slip distance $D_c = 1\text{e-}2$ m, reference friction coefficient $\mu_0 = 0.6$ and reference velocity $v_0 = 1\text{e-}9$ m/s. These parameters are homogenous over the fault zone and for all models, such that the fault is always velocity weakening with $a - b = -1.1\text{e-}2$. The static strength τ_s is the frictional strength prior to significant weakening, taken as the steady-state strength when $v_f = v_0$, giving $\tau_s = 60$ MPa. The dynamic frictional strength τ_f is calculated assuming steady-state sliding at a co-seismic velocity $v_c \sim 1$ m/s, giving $\tau_f = 37$ MPa and a maximum stress drop $\Delta\tau = \tau_s - \tau_f = 23$ MPa. The frictional parameters are chosen to give this stress drop and a sufficiently small nucleation length L_∞ to allow for small earthquakes to possibly nucleate (for shear modulus $G = 30$ GPa), given by (*59*):

$$L_\infty = \frac{2bGD_C}{\pi\sigma_{eff}(b-a)^2} = 316\ m \quad (15)$$

The length-scale over which localization due to frictional weakening occurs, called the process zone L_b, is approximate by (*59*):

$$L_b = \frac{GD_C}{b\sigma_{eff}} = 150\ m \quad (16)$$

Models are run for 2000 years, including a 500 year run-in period that is not included in analysis, which covers many earthquake cycles in all models. A model resolution of 29.3 m is chosen (modified to 97.7 m for the depth-dependent models), such that the nucleation length scale and process zone are resolved.

Measurement of model metrics

The maximum average shear stress τ_{max} is measured over the final 1000 years of the model run, in order to avoid the viscous relaxation that is still occurring at the start of some aseismic models (Fig. 2), though there is no discernible change in seismogenic behavior during this relaxation period. τ_{max} is chosen as the primary metric to characterize models as it corresponds to the pre-stress responsible for the largest events. It also reflects the tectonic loading stress, as it is limited by stress relaxation in these models (e.g. τ_{max} varies despite keeping frictional properties homogeneous and constant). Analysis of statistics in terms of the time-averaged fault shear stress give a similar trend over the full stress range, but with less variation between the most seismogenic models (Fig. S4) Analysis in terms of W shows the expected trend of increasing seismicity with decreasing W, but no clear correlations exist for the complete collection of model-sets, indicating that stress is the more generalized metric.

Events with $v_f > 10^{-2}$ m/s are identified as earthquakes and earthquake moment is calculated as $M_0 = \frac{1}{4} Gs\pi l_r^2$, for average slip s over a distance l_r and assuming a circular rupture area. Moment magnitude is then calculated as $M_w = \frac{2}{3}\log_{10} M_0 - 6.06$. The b-value is found by fitting the G-R

relationship to events with $M_w \geq 4$. Long-term seismic coupling χ is calculated by summing $sl_r/(v_p t l_{fault})$ over all events, for model duration t.

Calculation of b-values from effective asperity distributions and Monte Carlo simulation

We make simplified estimates of the b-value of earthquakes occurring on a fault with a given effective asperity distribution, by assuming each earthquake ruptures an asperity (defined as an area where $\eta v_p/W > \tau_s$) but does not propagate into the surrounding creeping region. A constant stress drop is assumed, such that rupture slip is proportional to rupture size:

$$s = \Delta\tau l_r/G \tag{17}$$

It is then assumed that $l_r = w_{eff}$ for effective asperity width w_{eff}. The number of events hosted on each asperity over a given time period varies, depending on asperity size, such that the loading rate can be accommodated. The number of events is then calculated as

$$N(w_{eff}) = \frac{t v_p G}{\Delta\tau w_{eff}} \tag{18}$$

Assuming a common stress drop $\Delta\tau$ =17 MPa given by the average stress drop in the reference model-set. We test the sensitivity of the b-value measurements of the QDYN earthquake cycle models, using a Monte Carlo simulation (dashed line and pink region in Fig. 4c). We generate randomized viscosity distributions, calculate the effective asperity distributions (in an identical manner to Fig. 3) for randomly generated driving stresses, and convert these to earthquake catalogues using Eq. (18) from which b-values are calculated.

Statistical sensitivity to the viscosity distribution

Four additional model-sets (Table 1) were run in order to test the sensitivity of our modelled earthquake statistics to the probability distribution used to generate the viscosity distribution. Model-sets B and C were identical to the reference model-set, however assuming a lower and higher η_{min} respectively, modifying the maximum viscosity contrasts. Model-set D replaced the uniform-logarithmic distribution (Eq. (14)) with a truncated power-law distribution with exponent D (*20*):

$$\eta = \left(\eta_{min}^{-D} + [\eta_{max}^{-D} - \eta_{min}^{-D}]\hat{X}\right)^{-\frac{1}{D}} \tag{19}$$

Model-set E instead assumed a bi-modal distribution, where η is randomly chosen to be either η_{min} or η_{max}. Each model-set is also repeated for three randomized patch distributions. Examples of each viscosity distribution are shown in Fig. S6.

Model-set	Viscosity Distribution	η_{min}(Pa s)	η_{max} (Pa s)	Total number of models
A (reference)	Logarithmic	10^{18}	10^{20}	21
B	Logarithmic	10^{19}	10^{20}	18
C	Logarithmic	10^{17}	10^{20}	12

D	Power-law	10^{18}	10^{20}	15
E	Bi-modal	10^{18}	10^{20}	15

Table 1. Summary of primary model-set parameters.

The trends of decreasing b-value and increasing χ and maximum M_w with increasing stress generally hold for these alternative viscosity distributions (Fig. 4). A lower viscosity contrast (model-set B) tends to result in the possibility of some relatively aseismic models at high stress (Fig. 4b), while a higher viscosity contrast (model-set C) makes little difference from the reference model-set. The power-law and bi-modal (model-sets D and E) distributions both result in a relatively sharp transition from aseismic to seismic behavior at around 45 MPa, without the smooth transition seen in the other models. The models with the bimodal distribution have a larger uncertainty in b-value measurement compared to other model-sets, as they deviate from the G-R relationship (large error-bars in Fig. 4c).

Single asperity rupture test models

A suite of simplified models were run to constrain how far a rupture can propagate through a creeping region, to provide further context for the primary model-set. A patch of high viscosity (10^{20} Pa s), with width w_a, was surrounded by homogenous material with viscosity η_m, assuming W=10 m (example model shown in Fig. S7). Both η_m and w_a were varied over 35 models, in order to explore their influence on rupture propagation distance into the creeping region (Fig. 6).

For most models, the rupture propagation is a small fraction of w_a, except for a subset of models where the rupture does not arrest and instead propagates across the entire fault. The rupture length primarily depends on $\bar{\tau}_0$, where τ_0 is taken as the matrix stress $\eta v_p/W$. Rupture propagation is limited to <1.5km when $\bar{\tau}_0 < 0.55$, while whole fault rupture can occur at $\bar{\tau}_0 > 0.55$ at a critical w_a (mostly still at the km scale) that decreases with increasing $\bar{\tau}_0$. This critical $\bar{\tau}_0$ corresponds to when stress is relaxed to 10 MPa below τ_s.

A simple energy balance model was calculated to further understand why rupture length is so limited at low $\bar{\tau}_0$, even for large patches. A rupture has a stress intensity factor K that evolves with rupture length and available stress drop (Fig. S8). Rupture arrest will occur if $K < K_c$. The critical stress intensity factor K_c is calculated as $K_c = \sqrt{2GD_c b\sigma_{eff}} \ln\left(\frac{v_{co}\theta_i}{D_c}\right)$, for co-seismic values of velocity and state variable, v_{co} and θ_i (taken from the numerical model). The stress intensity factor for a rupture of half length l_r propagating from a patch with uniform stress drop $\Delta\tau_a$ into a matrix of uniform available stress drop $\Delta\tau_m$ is:

$$K = \sqrt{\frac{\pi w_a}{2}}\left[\frac{2}{\pi}(\Delta\tau_a - \Delta\tau_m) arcsin\left(\frac{2l_r}{w_a}\right) + \Delta\tau_m\right] \quad (20)$$

Rupture arrest is then predicted at the l_r at which $K = \alpha K_c$, provided $\frac{\partial K}{\partial l_r} < 0$. α is a scale factor to incorporate differences between crack modes and deviations from the idealized crack-tip stress distribution, fit to the numerical data with $\alpha = 7.5$. For $w_a \gg L_\infty$, earthquake nucleation can occur without the entire patch reaching a critical stress, limiting $\Delta\tau_a$. Following Cattania (*21*), the stress intensity ahead of a creeping front loading the asperity is $K_{creep} = 2Gs/\left(\sqrt{2\pi l_r}\right)$. Rupture

nucleation will occur when $K_{creep} = K_c$, giving the critical displacement s for a given $l_r \approx w_a$. Combining with Eq. (17) gives a stress drop:

$$\Delta\tau_a = \sqrt{\frac{\pi}{2w_a}} K_c \tag{21}$$

The matrix is assumed to be creeping prior to earthquake nucleation, such that the maximum stress drop is $\Delta\tau_m = \frac{V_p \eta}{W} - \tau_d$.

The analytical solution is shown in Fig. 6 and predicts a plateau in rupture length with increasing w_a, as a result of the limited stress drop corresponding to partial patch ruptures. An increase in rupture length with increasing η_m is also predicted. However, the analytical solution overestimates the rupture length, particularly at high η. This overestimate is because stress shadows form at the patch edge, lowering the pre-seismic stress below that of viscous creep (Fig. S8; likely resulting in the high α).

Depth-dependent stress model

Two additional models are included where η is perturbed with depth, simulating a decrease in stress with depth as the influence of temperature-dependent creep increases. The model setup is identical to the reference model-set, but with a fault length of 100 km and a viscosity distribution that is scaled by a depth-dependent factor. The viscosity contrast, η_{max}/η_{min}, is held constant at 100. η_{min} and η_{max} are equally perturbed following a linearized form of the Arrhenius equation (for simplicity over the limited depth range), $\eta(z) = \min\left[\eta_o \exp\left(\alpha(z - z_0)\right), \eta_0\right]$, where η_0 is the original viscosity, z_0 is the onset of temperature dependence at a depth of 27.5 km and α is chosen to give a viscosity decrease of 1 order of magnitude over the model domain. With a geothermal gradient of 10^oC/km (typical of P-T conditions of exhumed samples thought to represent steady subduction, (*60*)) and activation energy Q = 135 kJ/mol (*61*), the Arrhenius temperature-dependence $\eta(T) = \eta_0 \exp\frac{Q}{RT}$ would give an order ~10^3 viscosity decrease over the lower half of the fault. The chosen factor of 10 decrease is then conservative, incorporating possible contrast reductions due to changing stress and deformation mechanism with depth. The effective normal stress and rate-and-state parameters are constant throughout the fault, for both simplicity and the former representing the role of fluid pressure feedbacks (*62*).

References

1. M. C. Gerstenberger, W. Marzocchi, T. Allen, M. Pagani, J. Adams, L. Danciu, E. H. Field, H. Fujiwara, N. Luco, K. F. Ma, C. Meletti, M. D. Petersen, Probabilistic Seismic Hazard Analysis at Regional and National Scales: State of the Art and Future Challenges. *Rev. Geophys.* **58**, 1–49 (2020).
2. S. L. Bilek, T. Lay, Subduction zone megathrust earthquakes. *Geosphere* (2018), doi:10.1130/GES01608.1.
3. Y. Y. Kagan, Seismic moment distribution revisited: I. Statistical results. *Geophys. J. Int.* **148**, 520–541 (2002).
4. M. Herrmann, W. Marzocchi, Inconsistencies and Lurking Pitfalls in the Magnitude–Frequency Distribution of High-Resolution Earthquake Catalogs. *Seismol. Res. Lett.* **92**, 909–922 (2020).
5. Z. H. El-Isa, D. W. Eaton, Spatiotemporal variations in the b-value of earthquake magnitude-frequency distributions: Classification and causes. *Tectonophysics*. **615**–**616**, 1–11 (2014).
6. C. H. Scholz, The frequency-magnitude relation of microfracturing in rock and its relation to earthquakes. *Bull. Seismol. Soc. Am.* (1968).
7. D. Schorlemmer, S. Wiemer, M. Wyss, Variations in earthquake-size distribution across different stress regimes. *Nature* (2005), doi:10.1038/nature04094.
8. M. Spada, T. Tormann, S. Wiemer, B. Enescu, Generic dependence of the frequency-size distribution of earthquakes on depth and its relation to the strength profile of the crust. *Geophys. Res. Lett.* (2013), doi:10.1029/2012GL054198.
9. T. Tormann, S. Wiemer, A. Mignan, Systematic survey of high-resolution b value imaging along Californian faults: Inference on asperities. *J. Geophys. Res. Solid Earth*. **119**, 2029–2054 (2014).
10. P. Nuannin, O. Kulhanek, L. Persson, Spatial and temporal b value anomalies preceding the devastating off coast of NW Sumatra earthquake of December 26, 2004. *Geophys. Res. Lett.* **32** (2005), doi:https://doi.org/10.1029/2005GL022679.
11. K. Mogi, Earthquakes and fractures. *Tectonophysics*. **5**, 35–55 (1967).
12. H. Kanamori, D. L. Anderson, Theoretical basis of some empirical relations in seismology. *Bull. Seismol. Soc. Am.* **65**, 1073–1095 (1975).
13. G. King, The accommodation of large strains in the upper lithosphere of the earth and other solids by self-similar fault systems: the geometrical origin of b-Value. *pure Appl. Geophys.* **121**, 761–815 (1983).
14. J. Huang, D. L. Turcotte, Fractal distributions of stress and strength and variations of b-value. *Earth Planet. Sci. Lett.* **91**, 223–230 (1988).
15. J. P. Ampuero, J. Ripperger, P. M. Mai, in *Geophysical Monograph Series* (2006).
16. P. Dublanchet, P. Bernard, P. Favreau, Interactions and triggering in a 3-D rate-and-state asperity model. *J. Geophys. Res. Solid Earth*. **118**, 2225–2245 (2013).
17. Z. Fang, E. M. Dunham, Additional shear resistance from fault roughness and stress levels on geometrically complex faults. *J. Geophys. Res. Solid Earth* (2013), doi:10.1002/jgrb.50262.
18. M. Galis, C. Pelties, J. Kristek, P. Moczo, J.-P. Ampuero, P. M. Mai, On the initiation of sustained slip-weakening ruptures by localized stresses. *Geophys. J. Int.* **200**, 888–907 (2015).
19. P. Dublanchet, Stress-Dependent b Value Variations in a Heterogeneous Rate-and-State Fault Model. *Geophys. Res. Lett.* (2020), doi:10.1029/2020GL087434.
20. M. P. A. van den Ende, J. Chen, A. R. Niemeijer, J. P. Ampuero, Rheological Transitions Facilitate Fault-Spanning Ruptures on Seismically Active and Creeping Faults. *J. Geophys. Res. Solid Earth*. **125**, 1–27 (2020).

21. C. Cattania, Complex Earthquake Sequences On Simple Faults. *Geophys. Res. Lett.* (2019), doi:10.1029/2019GL083628.
22. N. Coltice, M. Gérault, M. Ulvrová, A mantle convection perspective on global tectonics. *Earth-Science Rev.* (2017), , doi:10.1016/j.earscirev.2016.11.006.
23. S. Uyeda, H. Kanamori, Back-arc opening and the mode of subduction. *J. Geophys. Res.* (1979), doi:10.1029/jb084ib03p01049.
24. A. Dielforder, R. Hetzel, O. Oncken, Megathrust shear force controls mountain height at convergent plate margins. *Nature* (2020), doi:10.1038/s41586-020-2340-7.
25. R. H. Sibson, Frictional constraints on thrust, wrench and normal faults. *Nature*. **249**, 542–544 (1974).
26. J.-P. Avouac, From Geodetic Imaging of Seismic and Aseismic Fault Slip to Dynamic Modeling of the Seismic Cycle. *Annu. Rev. Earth Planet. Sci.* **43**, 233–271 (2015).
27. Fagereng, A. Beall, Is complex fault zone behaviour a reflection of rheological heterogeneity? *Philos. Trans. R. Soc. A Math. Phys. Eng. Sci.* **379** (2021), doi:10.1098/rsta.2019.0421.
28. J. P. Gratier, F. Thouvenot, L. Jenatton, A. Tourette, M. L. Doan, F. Renard, Geological control of the partitioning between seismic and aseismic sliding behaviours in active faults: Evidence from the Western Alps, France. *Tectonophysics*. **600**, 226–242 (2013).
29. C. D. Rowe, F. Meneghini, J. C. Moore, Textural record of the seismic cycle: strain-rate variation in an ancient subduction thrust. *Geol. Soc. London, Spec. Publ.* (2011), doi:10.1144/SP359.5.
30. M. Chlieh, J. P. Avouac, K. Sieh, D. H. Natawidjaja, J. Galetzka, Heterogeneous coupling of the Sumatran megathrust constrained by geodetic and paleogeodetic measurements. *J. Geophys. Res. Solid Earth* (2008), doi:10.1029/2007JB004981.
31. C. H. Scholz, J. Campos, The seismic coupling of subduction zones revisited. *J. Geophys. Res. Solid Earth*. **117** (2012), doi:10.1029/2011JB009003.
32. L. M. Wallace, Å. Fagereng, S. Ellis, Upper plate tectonic stress state may influence interseismic coupling on subduction megathrusts. *Geology*. **40**, 895–898 (2012).
33. B. M. Carpenter, C. Marone, D. M. Saffer, Weakness of the San Andreas Fault revealed by samples from the active fault zone. *Nat. Geosci.* **4**, 251–254 (2011).
34. B. Philibosian, A. J. Meltzner, Segmentation and supercycles: A catalog of earthquake rupture patterns from the Sumatran Sunda Megathrust and other well-studied faults worldwide. *Quat. Sci. Rev.* (2020), , doi:10.1016/j.quascirev.2020.106390.
35. A. Inbal, J. P. Ampuero, R. W. Clayton, *Science (80-.).*, in press, doi:10.1126/science.aaf1370.
36. Y. Luo, J. P. Ampuero, P. Galvez, M. van den Ende, B. Idini, QDYN: a Quasi-DYNamic earthquake simulator (v1.1) (2017), doi:10.5281/ZENODO.322459.
37. Å. Fagereng, R. H. Sibson, Mélange rheology and seismic style. *Geology*. **38**, 751–754 (2010).
38. B. Bos, C. J. Spiers, *J. Geophys. Res. Solid Earth*, in press, doi:https://doi.org/10.1029/2001JB000301.
39. A. Beall, Å. Fagereng, J. Huw Davies, F. Garel, D. Rhodri Davies, Influence of Subduction Zone Dynamics on Interface Shear Stress and Potential Relationship with Seismogenic Behavior. *Geochemistry, Geophys. Geosystems* (2021), doi:10.1029/2020gc009267.
40. R. E. Abercrombie, Earthquake source scaling relationships from −1 to 5 ML using seismograms recorded at 2.5-km depth. *J. Geophys. Res. Solid Earth*. **100**, 24015–24036 (1995).
41. T. Nishikawa, S. Ide, Earthquake size distribution in subduction zones linked to slab buoyancy. *Nat. Geosci.* (2014), doi:10.1038/ngeo2279.
42. A. Heuret, S. Lallemand, F. Funiciello, C. Piromallo, C. Faccenna, Physical characteristics

of subduction interface type seismogenic zones revisited. *Geochemistry, Geophys. Geosystems* (2011), doi:10.1029/2010GC003230.

43. J. Ripperger, J. P. Ampuero, P. M. Mai, D. Giardini, Earthquake source characteristics from dynamic rupture with constrained stochastic fault stress. *J. Geophys. Res. Solid Earth* (2007), doi:10.1029/2006JB004515.
44. J. D. Kirkpatrick, J. H. Edwards, A. Verdecchia, J. W. Kluesner, R. M. Harrington, E. A. Silver, Subduction megathrust heterogeneity characterized from 3D seismic data. *Nat. Geosci.* **13**, 369–374 (2020).
45. E. van Rijsingen, S. Lallemand, M. Peyret, D. Arcay, A. Heuret, F. Funiciello, F. Corbi, How Subduction Interface Roughness Influences the Occurrence of Large Interplate Earthquakes. *Geochemistry, Geophys. Geosystems* (2018), doi:10.1029/2018GC007618.
46. C. H. Scholz, On the stress dependence of the earthquake b value. *Geophys. Res. Lett.* (2015), doi:10.1002/2014GL062863.
47. J. C. Duarte, W. P. Schellart, A. R. Cruden, How weak is the subduction zone interface? *Geophys. Res. Lett.* (2015), doi:10.1002/2014GL062876.
48. W. D. Smith, The b-value as an earthquake precursor. *Nature*. **289**, 136–139 (1981).
49. T. H. W. Goebel, D. Schorlemmer, T. W. Becker, G. Dresen, C. G. Sammis, Acoustic emissions document stress changes over many seismic cycles in stick-slip experiments. *Geophys. Res. Lett.* (2013), doi:10.1002/grl.50507.
50. C. Marone, C. H. Scholz, The depth of seismic faulting and the upper transition from stable to unstable slip regimes. *Geophys. Res. Lett.* **15**, 621–624 (1988).
51. S. T. Tse, J. R. Rice, Crustal earthquake instability in relation to the depth variation of frictional slip properties. *J. Geophys. Res.* (1986), doi:10.1029/jb091ib09p09452.
52. N. Lapusta, J. R. Rice, Nucleation and early seismic propagation of small and large events in a crustal earthquake model. *J. Geophys. Res. Solid Earth*. **108**, 1–18 (2003).
53. D. L. Kohlstedt, B. Evans, S. J. Mackwell, Strength of the lithosphere: constraints imposed by laboratory experiments. *J. Geophys. Res.* (1995), doi:10.1029/95jb01460.
54. R. H. Sibson, Fault rocks and fault mechanisms. *J. Geol. Soc. London.* **133**, 191–213 (1977).
55. R. D. Hyndman, M. Yamano, D. A. Oleskevich, The seismogenic zone of subduction thrust faults. *Isl. Arc* (1997), doi:10.1111/j.1440-1738.1997.tb00175.x.
56. T. Nishimura, Y. Yokota, K. Tadokoro, T. Ochi, Strain partitioning and interplate coupling along the northern margin of the Philippine Sea plate, estimated from Global Navigation Satellite System and Global Positioning System-Acoustic data. *Geosphere*. **14**, 535–551 (2018).
57. M. Chlieh, J. P. Avouac, V. Hjorleifsdottir, T. R. A. Song, C. Ji, K. Sieh, A. Sladen, H. Hebert, L. Prawirodirdjo, Y. Bock, J. Galetzka, Coseismic slip and afterslip of the great Mw 9.15 Sumatra-Andaman earthquake of 2004. *Bull. Seismol. Soc. Am.* **97**, 152–173 (2007).
58. J. R. Rice, Y. Ben-Zion, Slip complexity in earthquake fault models. *Proc. Natl. Acad. Sci. U. S. A.* (1996), doi:10.1073/pnas.93.9.3811.
59. A. M. Rubin, J. P. Ampuero, Earthquake nucleation on (aging) rate and state faults. *J. Geophys. Res. Solid Earth* (2005), doi:10.1029/2005JB003686.
60. P. Agard, A. Plunder, S. Angiboust, G. Bonnet, J. Ruh, The subduction plate interface: rock record and mechanical coupling (from long to short timescales). *Lithos*. **320**–**321**, 537–566 (2018).
61. G. Hirth, C. Teyssier, W. J. Dunlap, An evaluation of quartzite flow laws based on comparisons between experimentally and naturally deformed rocks. *Int. J. Earth Sci.* **90**, 77–87 (2001).
62. J. R. Rice, Fault Stress States, Pore Pressure Distributions, and the Weakness of the San

Andreas Fault. *Int. Geophys.* **51**, 475–503 (1992).
63. C. R. Harris, K. J. Millman, S. J. van der Walt, R. Gommers, P. Virtanen, D. Cournapeau, E. Wieser, J. Taylor, S. Berg, N. J. Smith, R. Kern, M. Picus, S. Hoyer, M. H. van Kerkwijk, M. Brett, A. Haldane, J. F. del Río, M. Wiebe, P. Peterson, P. Gérard-Marchant, K. Sheppard, T. Reddy, W. Weckesser, H. Abbasi, C. Gohlke, T. E. Oliphant, Array programming with NumPy. *Nature*. **585**, 357–362 (2020).
64. J. D. Hunter, Matplotlib: A 2D graphics environment. *Comput. Sci. Eng.* **9**, 90–95 (2007).

Acknowledgments

Data analysis and plotting used the NumPy (*63*) and Matplotlib (*64*) Python libraries. AB thanks A.Rubin for helpful discussions.

Funding:

European Union's Horizon 2020 research and innovation program, starting Grant Agreement 715836 MICA (AB, ÅF).
French government supported UCA^{JEDI} Investments in the Future project managed by the National Research Agency (ANR) grant ANR-15-IDEX-01 (MPAvdE).
3IA Côte d'Azur Investments in the Future project grant ANR-19-P3IA-0002 (MPAvdE).

Author contributions:

Conceptualization: AB
Design and implementation of visco-frictional numerical modelling method: MPAvdE
Model design: AB, MPAvdE
Model runs, data analysis and visualization: AB
Writing - original draft: AB
Writing - review and editing: AB, MPAvdE, JPA, ÅF

Competing interests: Authors declare that they have no competing interests.

Data and materials availability: All data needed to evaluate and reproduce our methods and findings are described in the paper and Supplementary Materials. QDYN is publicly available at https://github.com/ydluo/qdyn. An unreleased version incorporating the visco-frictional rheology is available at https://github.com/ydluo/qdyn/tree/feature/viscosity and readers are recommended to contact the authors for further information on its use.